

Chapter 2

Probing and Controlling Quantum Matter Using Ultracold Quantum Gases in Optical Lattices

Immanuel Bloch

Abstract These lecture notes provide an introduction into the field of strong correlation physics with ultracold atoms in optical lattices. After a basic introduction into the single particle bandstructure and lattice configurations, the effect of strong interactions in the Hubbard model are discussed. Detection methods are introduced, which allow one to reveal in-trap density and (quasi)-momentum distributions, as well as correlations between particles on the lattice. The fundamental phases of the bosonic and fermionic Hubbard model are discussed. Superexchange spin-spin interactions that form the basis of quantum magnetism are introduced and the current status on observing such magnetic phenomena are highlighted. Finally, the novel possibilities to detect and control individual atoms on single lattice sites are outlined.

1 Introduction

Ultracold quantum gases in optical lattices have become a major research area in the field of atomic and molecular quantum gases. Not only do they allow one to investigate prototypical condensed matter Hamiltonians, but they also offer the possibility to reach novel physical regimes, which are in many cases unattainable in real condensed matter systems [1–4]. Optical lattices are generally formed by interfering several laser beams and the resulting intensity of the interference pattern is experienced by the atoms as a light induced potential via their polarizability. The dimensionality of such a lattice and its geometry can be fully controlled through the amplitude and the directions of the interfering laser beams. Interactions can be tuned via Feshbach resonances [5] or by quenching kinetic energy when going to deeper

I. Bloch (✉)

Max Planck Institute of Quantum Optics, 85748 Garching, Germany

I. Bloch

Ludwig-Maximilians-University, 80799 Munich, Germany

e-mail: immanuel.bloch@mpq.mpg.de

lattices. Ultracold atoms in optical lattices have thus become a powerful setting for investigating strongly correlated quantum gases. They also offer a new window for the observation of non-equilibrium dynamics in quantum many-body systems [6], where timescales and dynamical evolutions are conveniently in the regime of milliseconds rather than femtoseconds.

The present lecture notes represent an introduction into the field of optical lattices and cover some of the basics in (a) the generation of optical lattices, (b) the detection methods employed to image in-situ and momentum distributions and (c) discuss some of the many-body phases that have been investigated in this context. In the last part of the manuscript, the novel single-site and single-atom resolved detection techniques are introduced that have opened a new window for investigating quantum gases in optical lattices with unprecedented resolution down to the level of revealing individual thermal or quantum fluctuations in the system. The notes are far from a complete survey of what has been done in the field, but rather represent a selection of introductory topics with references to more detailed discussions throughout the text.

2 Fundamentals of Optical Lattices

Atoms may be trapped in standing wave light fields by exploiting the so called optical dipole force. The basic mechanism underlying such dipole traps may be explained via a simple semiclassical picture: the oscillating electric field of a laser induces an oscillating electric dipole in an atom. This atomic dipole can again interact with the external field, thereby creating a potential for an atom that is proportional to the intensity of the applied laser light. For laser-light with a frequency below an atomic transition frequency $\omega_L < \omega_0$ (red detuning), the atomic dipole oscillates in-phase with the applied electric field, whereas for blue-detuning $\omega_L > \omega_0$ it oscillates out-of-phase. This results in an attractive (repulsive) induced dipole potential for the case of red (blue) detuning [7].

2.1 Optical Lattices

Periodic potentials based on dipole forces can be formed by overlapping two counterpropagating laser beams. Due to the interference between the two light fields, an optical standing wave with period $\lambda/2$ is formed, in which the atoms can be trapped. More generally, by choosing the two laser beams to interfere under an angle less than 180° , one can also realize periodic potentials with a larger period [8, 9]. For counterpropagating gaussian laser beams, the resulting trapping potential is of the form

$$V(r, z) = -V_0 \cdot e^{-2r^2/w^2(z)} \cdot \sin^2(kz) \quad (1)$$

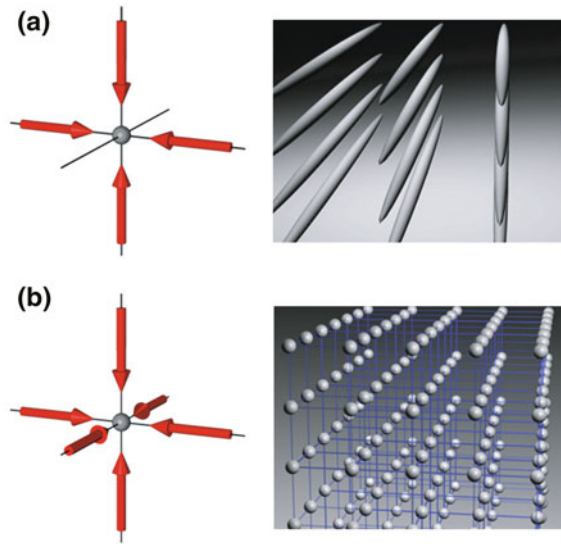


Fig. 1 Two-dimensional (a) and three-dimensional (b) optical lattice potentials formed by superimposing two or three orthogonal standing waves. For a two-dimensional optical lattice, the atoms are confined to an array of tightly confining one-dimensional potential tubes, whereas in the three-dimensional case the optical lattice can be approximated by a three dimensional simple cubic array of tightly confining, harmonic oscillator potentials at each lattice site

where $k = 2\pi/\lambda$ is the wave vector of the laser light and V_0 denotes the depth of the lattice potential.

Periodic potentials in two or three dimensions can be formed by overlapping two or three optical standing waves along different, usually orthogonal, directions. For orthogonal polarization vectors or different frequencies of the individual standing waves, the resulting optical potential in the centre of the trap is then a simple sum of purely sinusoidal potentials in two- or three directions.

In two-dimensional optical lattice potential, the atoms are confined to arrays of tightly confining one-dimensional tubes (see Fig. 1a). For typical experimental parameters the harmonic trapping frequencies along the tube are very weak and on the order of 10–200 Hz, while in the radial direction the trapping frequencies can become as high as 100 kHz. For sufficiently deep lattice depths, atoms can thus move only axially along the tube. In this manner, it is possible to realize quantum wires with neutral atoms, which allow to study strongly correlated gases in one dimension. Arrays of such quantum wires have been realized by several groups [10–14].

In case of three dimensional lattice potentials, the confinement on a single lattice site is approximately harmonic. The atoms are then tightly confined at a single lattice site, with trapping frequencies ω_0 of up to $2\pi \times 100$ kHz. The energy $\hbar\omega_0 = 2E_r (V_0/E_r)^{1/2}$ of local oscillations in the well is on the order of several

recoil energies $E_r = \hbar^2 k^2 / 2m$, which is a natural measure of energy scales in optical lattice potentials. Typical values of E_r are in the range of several kHz for ^{87}Rb .

2.2 Tight Binding Regime

For sufficiently deep lattices above $V_0 \gtrsim 5E_r$, quantum gases on a lattice are well described within a tight binding approximation. If the interaction energy between particles is in addition smaller than the separation between the lowest and higher energy bands, then we may restrict our discussion to particles only occupying a single energy band in the lattice—the lowest Bloch band. For neutral atoms interacting via short ranged molecular potentials, this is the typical situation encountered in experiments and the one we shall focus on in the discussion below.

Kinetic Energy The movement of particles on a lattice is under such conditions simply given by the hopping between neighboring lattice sites

$$H = -J \sum_{\langle \mathbf{R}, \mathbf{R}' \rangle} \hat{a}_{\mathbf{R}, \sigma}^\dagger \hat{a}_{\mathbf{R}', \sigma}, \quad (2)$$

where $\hat{a}_{\mathbf{R}', \sigma}$ denotes the fermionic (bosonic) particle destruction operator on lattice site \mathbf{R}' . The parameter $J > 0$ is the gain in kinetic energy due to nearest neighbor tunneling. In the limit $V_0 \gg E_r$, it can be obtained from the width $W \rightarrow 4J$ of the lowest band in the 1D Mathieu-equation:

$$J = \frac{4}{\sqrt{\pi}} E_r \left(\frac{V_0}{E_r} \right)^{3/4} \exp -2 \left(\frac{V_0}{E_r} \right)^{1/2}. \quad (3)$$

For static lattice potentials $J > 0$, however, recently it has been shown that by time-modulation of the lattice potential position, one can also access regimes, where effectively, after time-averaging, $J < 0$ [15, 16].

Interaction Energy For typical short-ranged collisional interactions between the particles, the interaction energy between two atoms can be described by an onsite interaction energy, typical of the form in Hubbard models:

$$H_{\text{int}}^B = \frac{1}{2} U \sum_{\mathbf{R}} \hat{n}_{\mathbf{R}} (\hat{n}_{\mathbf{R}} - 1) \quad \text{and} \quad H_{\text{int}}^F = U \sum_{\mathbf{R}} \hat{n}_{\mathbf{R}, \sigma} \hat{n}_{\mathbf{R}, \sigma'} \quad (4)$$

For single species bosons or fermions in different spin states σ and σ' , respectively. Within the pseudopotential approximation for the interactions between the particles, the onsite interaction energy U is given by:

$$U = g \int d^3r |w(\mathbf{r})|^4 = \sqrt{\frac{8}{\pi}} ka E_r \left(\frac{V_0}{E_r} \right)^{3/4} \quad (5)$$

Here a denotes the s -wave scattering length between two atoms and $w(\mathbf{r})$ is the Wannier function on a lattice site. Longer ranged interactions could be generated by making use of long-ranged dipolar interactions in polar molecules [17] or ground state atoms dressed with a small Rydberg state admixture [18–20]. For collisional interactions alone, the description of the interactions as local onsite interactions, is, however, an excellent approximation.

Trapping Potential Typically an overall harmonic trapping potential is used to confine the quantum gases to a trapping region. In a lattice, this gives rise to an additional term in the Hamiltonian of the form (in 1D):

$$H_{\text{trap}} = V_t \sum_{\mathbf{R}, \sigma} \mathbf{R}^2 \hat{n}_{\mathbf{R}, \sigma}, \quad (6)$$

where \mathbf{R} denotes the position of the \mathbf{R} th lattice site. While the trapping potential is typically weak compared to the lattice potential and the corresponding characteristic length scale is long compared to the lattice period, the overall harmonic confinement has profound implications for resulting quantum phases in the trap. This can best be understood by introducing a local chemical potential $\mu_{\text{loc}}(\mathbf{R}) = \mu - V_t \mathbf{R}^2$ (for $\mu_{\text{loc}}(\mathbf{R}) > 0$, else $\mu_{\text{loc}}(\mathbf{R}) = 0$). Within a local density approximation (LDA) the inhomogeneous trapped quantum gas behaves locally as a homogeneous system with chemical potential μ_{loc} . As one moves from the center of the trapped gas radially outwards to its border, one thus samples many-body phases at different chemical potentials $0 < \mu_{\text{loc}} < \mu$. In contrast to a homogeneous sample, where the system exhibits a single quantum phase, trapped quantum gases therefore typically exhibit several coexisting quantum phases in the trap. Although there are cases where such coexisting phases can complicate the analysis of the system, the harmonic trapping potential generally facilitates the generation of many-body quantum phases with ultracold atoms, as we will show in the case of Hubbard type model systems. The approximation of the trapped quantum gas via LDA is expected to fail close to a quantum critical point, where the length scale of the fluctuating region tends to diverge [21].

2.3 Non-Standard Lattice Configurations

We have seen that by overlapping optical standing waves orthogonally to each other, one can create lattice potentials of simple cubic symmetry. Almost any other symmetry maybe be created via Fourier synthesis, i.e. superimposing standing waves of different wavelengths under different angles. Next to simple cubic type potentials, triangular, hexagonal [22] or Kagomé [23] lattice potentials have also been realized or proposed for ultracold atoms.

Spin-Dependent Lattices When using laser light, detuned not too far from a set of excited sublevels (for example for alkalis, the detuning should be close to the fine-structure splitting), one may also realize lattice potentials, which can be vastly different for different spin states of an atom or molecule. A prominent example in this respect are spin-dependent potentials that can be realized using counter-propagating laser beams with an angle θ between the two linear polarizations of the counter-propagating light fields [24–26]. Such a configuration can be described by two σ^+ and σ^- polarized standing waves, whose relative position to each other $\Delta x = \theta/\pi \times (\lambda/2)$ can be set by the angle θ . Shifting the two lattices relative to each other allows one to tune the interaction matrix element $U_{\uparrow\downarrow}$ between two spin components without the use of Feshbach resonances, but rather by changing the wave-function overlap of the spin-components on a lattice site.

Optical Superlattices When superimposing two standing wave light fields with exactly a factor of two difference between the two underlying lasers, optical superlattices can be created. Such optical superlattices mimic arrays of double wells, where the interwell and intrawell barrier of the double wells can be controlled dynamically and *in-situ* by changing the frequency and amplitude of the two light fields relative to each other. Such optical superlattices have been successfully used to detect onsite exchange [27] and next neighbor superexchange interactions [28] that will be discussed in Sect. 5. Extending such superlattices along two orthogonal directions, enables one to realize systems of coupled plaquettes [29, 30] that can be useful to investigate plaquette superfluidity or access low-entropy *d*-wave superfluids in an adiabatic manner [31, 32].

3 Detection Methods

The standard way of probing quantum gases has been connected to time-of-flight methods. Atoms are suddenly released from the trapping potential and subsequently imaged after a variable expansion time in free space. In the context of optical lattice quantum gases, such a time-of-flight image yields useful information about the momentum distribution and thereby coherence properties of the quantum gas. By adiabatically turning off the lattice, one may image the quasi-momentum distribution in the lattice rather than the momentum distribution. Both methods are discussed below in detail, as well as the possibility to use a noise-correlation analysis of time-of-flight images to learn about the correlation properties of the gas. More recently developed in-situ and single-site resolved imaging techniques are discussed in the separate Chap. 6.

3.1 Time-of-Flight Imaging and Adiabatic Mapping

Sudden release When releasing ultracold quantum gases from an optical lattice, two possible release methods can be chosen. If the lattice potential is turned off abruptly and interaction effects can be neglected, a given Bloch state with quasi-momentum

q will expand according to its momentum distribution as a superposition of plane waves with momenta $p_n = \hbar q \pm n \times 2\hbar k$. This is a direct consequence of the fact that Bloch waves can be expressed as a superposition of plane wave states $\exp i(\mathbf{q} + \mathbf{G}) \cdot \mathbf{r}$ with momenta $\mathbf{q} + \mathbf{G}$, which include arbitrary reciprocal lattice vectors \mathbf{G} . In a simple cubic lattice with lattice spacing $d = \pi/k$, the vectors \mathbf{G} are integer multiples of the fundamental reciprocal lattice vector $2k$. After a certain time-of-flight time, this momentum distribution can be imaged using standard absorption imaging methods. If only a single Bloch state is populated, as is the case for a Bose-Einstein condensate with quasi-momentum $q = 0$, this results in a series of interference maxima that can be observed after a time-of-flight period t . The density distribution observed after a fixed time-of-flight at position \mathbf{x} , is nothing but the momentum distribution of the particles trapped in the lattice

$$n(\mathbf{x}) = \left(\frac{m}{\hbar t}\right)^3 |\tilde{w}(\mathbf{k})|^2 \mathcal{G}(\mathbf{k}). \quad (7)$$

Here \mathbf{k} is related to \mathbf{x} by $\mathbf{k} = m\mathbf{x}/\hbar t$ due to the assumption of ballistic expansion while $\tilde{w}(\mathbf{k})$ is the Fourier transform of the Wannier function. The coherence properties of the many-body state are characterized by the Fourier transform

$$\mathcal{G}(\mathbf{k}) = \sum_{\mathbf{R}, \mathbf{R}'} e^{i\mathbf{k} \cdot (\mathbf{R} - \mathbf{R}')} G^{(1)}(\mathbf{R}, \mathbf{R}') \quad (8)$$

of the one-particle density matrix $G^{(1)}(\mathbf{R}, \mathbf{R}') = \langle \hat{a}_{\mathbf{R}}^\dagger \hat{a}_{\mathbf{R}'} \rangle$.

In a BEC, the long range order in the amplitudes leads to a constant value of the first order coherence function $G^{(1)}(\mathbf{R}, \mathbf{R}')$ at large separations $|\mathbf{R} - \mathbf{R}'|$. The resulting momentum distribution coincides with the standard multiple wave interference pattern obtained with light diffracting off a material grating. The atomic density distribution observed after a long enough time-of-flight time, thus yields information on the coherence properties of the many-body system [33, 34].¹

Adiabatic mapping One of the advantages of using optical lattice potentials is that the lattice depth can be dynamically controlled by simply tuning the laser power. This opens another possibility for releasing the atoms from the lattice potential e.g. by adiabatically converting a deep optical lattice into a shallow one and eventually completely turning off the lattice potential. Under adiabatic transformation of the lattice depth, the quasi-momentum \mathbf{q} is preserved and during the turn off process a Bloch wave in the n th energy band is mapped onto a corresponding free particle momentum \mathbf{p} in the n th Brillouin zone (see Fig. 2) [10, 35, 36].

The adiabatic mapping technique has been applied to the case of bosonic [10] and fermionic [36] atoms. For the situation of a homogeneously filled lowest energy band, an adiabatic ramp down of the lattice potential leaves the central Brillouin zone—a square of width $2\hbar k$ —fully occupied (see Fig. 3b). If on the other hand higher energy

¹ If interaction effects occur during time-of-flight expansion, the observed density distribution can deviate from the in-trap momentum distribution.

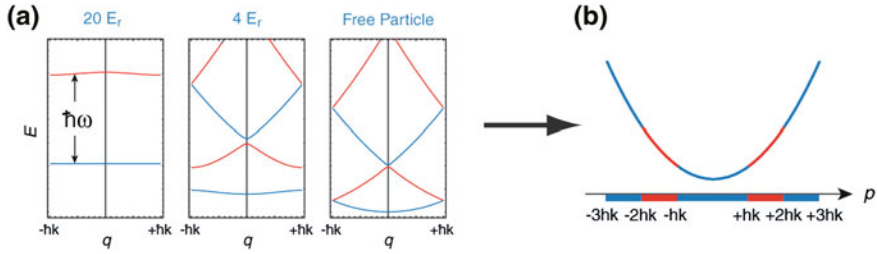


Fig. 2 **a** Bloch bands for different potential depths. During an adiabatic ramp down the quasi momentum is conserved and **b** a Bloch wave with quasi momentum q in the n th energy band is mapped onto a free particle with momentum p in the n th Brillouin zone of the lattice

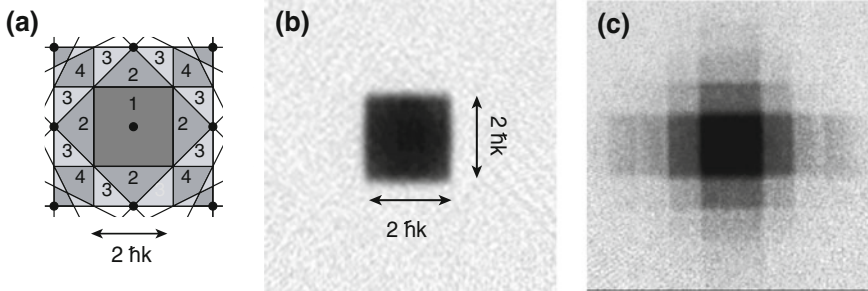


Fig. 3 **a** Brillouin zones of a 2D simple cubic optical lattice. For a homogeneously filled lowest Bloch band, an adiabatic shut off of the lattice potential leads to a homogeneously populated first Brillouin zone, which can be observed through absorption imaging after a time-of-flight expansion **(b)**. If in addition higher Bloch bands were populated, higher Brillouin zones become populated as well **(c)**

bands are populated, one also observes populations in higher Brillouin zones (see Fig. 3c). As in this method each Bloch wave is mapped onto a specific free-particle momentum state, it can be used to efficiently probe the distribution of the particles over Bloch states in different energy bands [10, 35–37].

3.2 Time-of-Flight Versus Noise Correlations

Let us begin by considering a quantum gas released from a trapping potential. After a finite time-of-flight time t , the resulting density distribution yields a three-dimensional density distribution $n_{3D}(\mathbf{x})$. If interactions can be neglected during time-of-flight, the average density distribution is related to the in-trap quantum state via:

$$\begin{aligned}\langle \hat{n}_{3D}(\mathbf{x}) \rangle_{\text{tof}} &= \langle \hat{a}_{\text{tof}}^\dagger(\mathbf{x}) \hat{a}_{\text{tof}}(\mathbf{x}) \rangle_{\text{tof}} \\ &\approx \langle \hat{a}^\dagger(\mathbf{k}) \hat{a}(\mathbf{k}) \rangle_{\text{trap}} = \langle \hat{n}_{3D}(\mathbf{k}) \rangle_{\text{trap}},\end{aligned}\quad (9)$$

where \mathbf{k} and \mathbf{x} are related by the ballistic expansion condition $\mathbf{k} = M\mathbf{x}/\hbar t$ (a factor $(M/\hbar t)^3$ from the transformation of the volume elements $d^3x \rightarrow d^3k$ is omitted). Here we have used the fact that for long time-of-flight times, the initial size of the atom cloud in the trap can be neglected. It is important to realize, that in each experimental image, a single realization of the density is observed, not an average. Moreover, each pixel in the image records on average a substantial number N_σ of atoms. For each of those pixels, however, the number of atoms recorded in a *single realization* of an experiment will exhibit shot noise fluctuations of relative order $1/\sqrt{N_\sigma}$ which will be discussed below. As shown in Eq. (9), the density distribution after time-of-flight represents a momentum distribution reflecting the first order coherence properties of the in-trap quantum state. This assumption is however only correct, if during the expansion process interactions between the atoms do not modify the initial momentum distribution, which we will assume throughout the text. When the interactions between the atoms have been enhanced, e.g. by a Feshbach resonance, or a high density sample is prepared, such an assumption is not always valid. Near Feshbach resonances one therefore often ramps back to the zero crossing of the scattering length before expansion.

Density-density correlations in time-of-flight images Let us now turn to the observation of density-density correlations in the expanding atom clouds [38]. These are characterized by the density-density correlation function

$$\langle \hat{n}(\mathbf{x}) \hat{n}(\mathbf{x}') \rangle = \langle \hat{n}(\mathbf{x}) \rangle \langle \hat{n}(\mathbf{x}') \rangle g^{(2)}(\mathbf{x}, \mathbf{x}') + \delta(\mathbf{x} - \mathbf{x}') \langle \hat{n}(\mathbf{x}) \rangle \quad (10)$$

which contains the normalized pair distribution $g^{(2)}(\mathbf{x}, \mathbf{x}')$ and a self correlation term. Relating the operators after time-of-flight expansion to the in-trap momentum operators, using Eq. (9), one obtains:

$$\begin{aligned}\langle \hat{n}_{3D}(\mathbf{x}) \hat{n}_{3D}(\mathbf{x}') \rangle_{\text{tof}} &\approx \langle \hat{a}^\dagger(\mathbf{k}) \hat{a}(\mathbf{k}) \hat{a}^\dagger(\mathbf{k}') \hat{a}(\mathbf{k}') \rangle_{\text{trap}} = \\ &\langle \hat{a}^\dagger(\mathbf{k}) \hat{a}^\dagger(\mathbf{k}') \hat{a}(\mathbf{k}') \hat{a}(\mathbf{k}) \rangle_{\text{trap}} + \delta_{\mathbf{k}\mathbf{k}'} \langle \hat{a}^\dagger(\mathbf{k}) \hat{a}(\mathbf{k}) \rangle_{\text{trap}}.\end{aligned}\quad (11)$$

The last term on the rhs of the above equation is the autocorrelation term and will be dropped in the subsequent discussion, as it only contributes to the signal for $\mathbf{x} = \mathbf{x}'$ and contains no more information about the initial quantum state, than the momentum distribution itself. The first term, however, shows that for $\mathbf{x} \neq \mathbf{x}'$, subtle momentum-momentum correlations of the in-trap quantum states are present in the noise-correlation signal of the expanding atom clouds.

Let us discuss the obtained results for two cases that have been analyzed in the experiment: (1) Ultracold atoms in a Mott insulating state or a fermionic band insulating state released from a 3D optical lattice and (2) two interfering one-dimensional quantum gases separated by a distance \mathbf{d} .

3.2.1 Noise Correlations in Bosonic Mott and Fermionic Band Insulators

Consider a bosonic Mott insulating state or a fermionic band insulator in a three-dimensional simple cubic lattice. In both cases, each lattice site \mathbf{R} is occupied by a fixed atom number $n_{\mathbf{R}}$. Such a quantum gas is released from the lattice potential and the resulting density distribution is detected after a time-of-flight t . In a deep optical lattice, the (in-trap) field operator $\hat{\psi}(\mathbf{r})$ can be expressed as a sum over destruction operators $\hat{a}_{\mathbf{R}}$ of localized Wannier states and neglecting all but the lowest band. The field operator for destroying a particle with momentum \mathbf{k} is therefore given by

$$\hat{a}(\mathbf{k}) = \int e^{-i\mathbf{k}\mathbf{r}} \hat{\psi}(\mathbf{r}) d^3r \simeq \tilde{w}(\mathbf{k}) \sum_{\mathbf{R}} e^{-i\mathbf{k}\mathbf{R}} \hat{a}_{\mathbf{R}}, \quad (12)$$

where $\tilde{w}(\mathbf{k})$ denotes the Wannier function in momentum space.

For the two states considered here, the expectation value in Eq. (11) factorizes into one-particle density matrices $\langle \hat{a}_{\mathbf{R}}^\dagger \hat{a}_{\mathbf{R}'} \rangle = n_{\mathbf{R}} \delta_{\mathbf{R}, \mathbf{R}'}$ with vanishing off-diagonal order. The density-density correlation function after a time-of-flight is then given by (omitting the autocorrelation term of order $1/N$)

$$\begin{aligned} \langle \hat{n}_{3D}(\mathbf{x}) \hat{n}_{3D}(\mathbf{x}') \rangle &= |\tilde{w}(M\mathbf{x}/\hbar t)|^2 |\tilde{w}(M\mathbf{x}'/\hbar t)|^2 N^2 \\ &\times \left[1 \pm \frac{1}{N^2} \left| \sum_{\mathbf{R}} e^{i(\mathbf{x}-\mathbf{x}') \cdot \mathbf{R}(M/\hbar t)} n_{\mathbf{R}} \right|^2 \right]. \end{aligned} \quad (13)$$

The plus sign in the above equation corresponds to the case of bosonic particles and the minus sign to the case of fermionic particles in a lattice. Both in a Mott state of bosons and in a filled band of fermions, the local occupation numbers $n_{\mathbf{R}}$ are fixed integers. The above equation then shows that correlations or anticorrelations in the density-density expectation value appear for bosons or fermions, whenever the difference $\mathbf{k} - \mathbf{k}'$ is equal to a reciprocal lattice vector \mathbf{G} of the underlying lattice. In real space, where the images are actually taken, this corresponds to spatial separations for which

$$|\mathbf{x} - \mathbf{x}'| = \ell = \frac{2\hbar t}{\lambda M}. \quad (14)$$

Such spatial correlations or anticorrelations in the quantum noise of the density distribution of expanding atom clouds can in fact be traced back to the famous Hanbury Brown and Twiss effect [39–41] and its analogue for fermionic particles [42–47]. For the case of two atoms localized at two lattice sites this can be readily understood in the following way: there are two possible ways for the particles to reach two detectors at positions \mathbf{x} and \mathbf{x}' which differ by exchange. A constructive interference for the case of bosons or a destructive interference for the case of fermions then leads to correlated or anticorrelated quantum fluctuations that are registered in the density-density correlation function [38, 41].

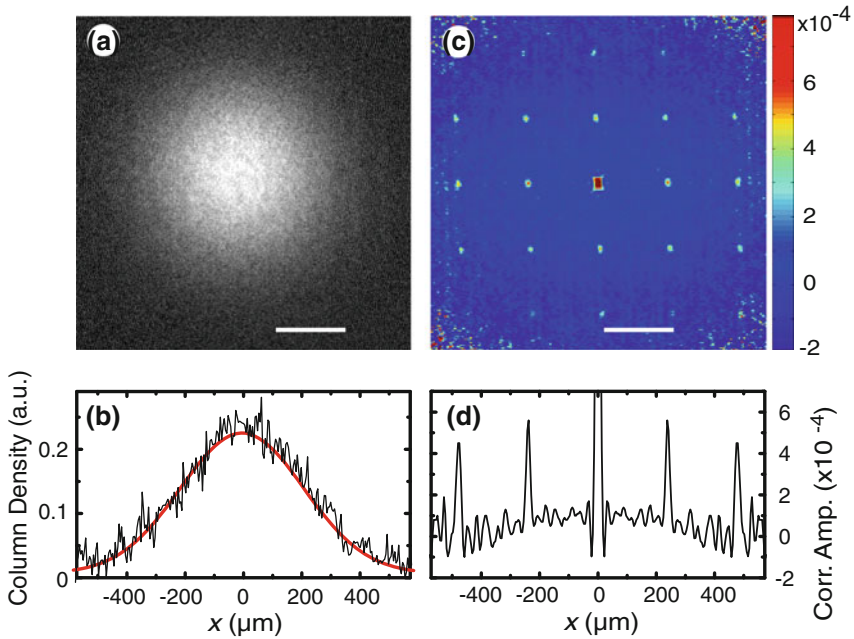


Fig. 4 Noise correlations of a Mott insulator released from a 3D optical lattice. **a** Single shot absorption image of a Mott insulator released from an optical lattice and associated cut through the image **(b)**. A statistical correlation analysis over several independent images such as the one in **a** yields the correlation function **(c)**. A cut through this two-dimensional correlation function reveals a Hanbury-Brown and Twiss type bunching of the bosonic atoms **(d)**. Adapted from Fölling et al. [48]

The correlations for the case of a bosonic Mott insulating state and anticorrelations for the case of a fermionic band insulating state have recently been observed experimentally [46, 48, 49]. In these experiments several single images of the desired quantum state are recorded after releasing the atoms from the optical trapping potential and observing them after a finite time-of-flight time (for a single of these images see e.g. Figs. 4a or 5a). These individually recorded images only differ in the atomic shot noise from each other. A set of such absorption images is then processed to yield the spatially averaged second order correlation function $g_{\text{exp}}^{(2)}(\mathbf{b})$:

$$g_{\text{exp}}^{(2)}(\mathbf{b}) = \frac{\int \langle n(\mathbf{x} + \mathbf{b}/2) \cdot n(\mathbf{x} - \mathbf{b}/2) \rangle d^2\mathbf{x}}{\int \langle n(\mathbf{x} + \mathbf{b}/2) \rangle \langle n(\mathbf{x} - \mathbf{b}/2) \rangle d^2\mathbf{x}}. \quad (15)$$

As shown in Fig. 4, the Mott insulating state exhibits long range order in the pair correlation function $g^{(2)}(\mathbf{b})$. This order is not connected with the trivial periodic modulation of the average density imposed by the optical lattice after time-of-flight, which is factored out in $g^{(2)}(\mathbf{x}, \mathbf{x}')$ (see Eq. (10)). Therefore, in the superfluid regime, one expects $g^{(2)}(\mathbf{x}, \mathbf{x}') \equiv 1$ despite the periodic density modulation in the interference

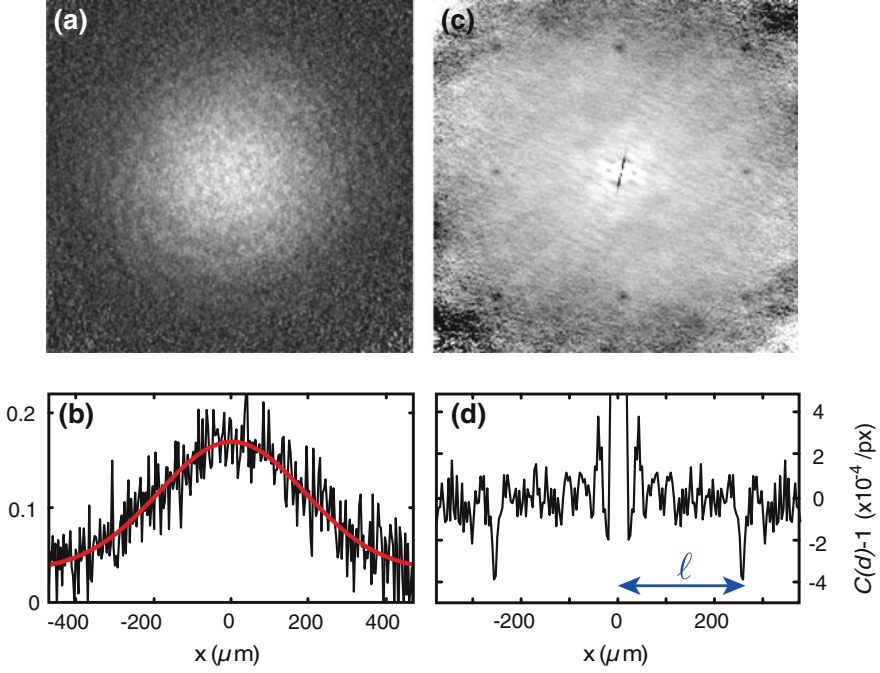


Fig. 5 Noise correlations of a band insulating Fermi gas. Instead of the correlation bunching peaks observed in Fig. 4 the fermionic quantum gas shows an HBT type antibunching effect, with dips in the observed correlation function. Adapted from Rom et al. [46]

pattern after time-of-flight. It is interesting to note that the correlations or anticorrelations can also be traced back to the enhanced fluctuations in the population of the Bloch waves with quasi momentum q for the case of the bosonic particles and the vanishing fluctuations in the population of Bloch waves with quasi momentum q for the case of fermionic particles [46].

Note that in general the signal amplitude obtained in the experiments for the correlation function deviates significantly from the theoretically expected value of one. In fact, one typically observes signal levels of 10^{-4} – 10^{-3} (see Figs. (4 and 5)). This can be explained by the finite optical resolution when imaging the expanding atomic clouds, thus leading to a broadening of the detected correlation peaks and thereby a decreased amplitude, as the signal weight in each correlation peak is preserved in the detection process. Using single atom detectors with higher spatial and temporal resolution such as the ones used in [47, 50], one can overcome such limitations and thereby also evaluate higher order correlation functions.

4 Bose and Fermi Hubbard Models

The single band Hubbard models play a paramount role in the context of condensed matter physics. Although they are among the simplest models used to describe interacting particles on a lattice, in several cases not even the phase diagram of the system is known and analytical solutions of the Hubbard model have not yet been found. In the case of the fermionic Hubbard model, it is also widely believed that it contains the essential physics for the explanation of high-temperature superconductivity [51, 52]. The fact that both models can be realized efficiently with ultracold atoms [53, 54] and the fact that all the underlying parameters of the Hubbard model may be tuned and controlled in cold atom and molecule experiments, has led to widespread interest of ultracold gases as efficient quantum simulators of these foundational Hamiltonians [1–3]. Current research is driven by the quest to explore the low temperature (entropy) phases of these models, but has also opened a new path to studying non-equilibrium phenomena in strongly correlated quantum systems beyond linear response [6].

As one of the most striking phenomena in both the case of bosons and fermions, for strong repulsive interactions between the particles compared to their kinetic energy $U \gg J$ and integer fillings, the many-body system forms a Mott insulating state, with strongly suppressed density fluctuations. Mott insulators form the basis for states with magnetic order, when the temperature of the system becomes sufficiently lower than the superexchange coupling between two spin states on neighboring lattice sites. The quest to realize such magnetically ordered states and the novel possibilities offered by ultracold atoms and molecules is discussed in the subsequent chapters.

Before we proceed, we will need to discuss a fundamental difference between a typical condensed matter and cold quantum gas experiment. Typical condensed matter experiments are carried out under conditions where a probe sample is held at a constant temperature through a connection to a reservoir. Lowering the temperature then allows one to access novel phases of the many-body system. In the context of ultracold quantum gases, we are dealing with quantum systems that are completely isolated from their environment. A change of the underlying trapping or lattice parameters typically also leads to a change in the temperature of the isolated gas. A temperature reduction caused by a trap deformation for example, might not bring one any closer to the transition point of a new phase, as the associated transition temperature typically is lowered as well. A much more useful system variable that is invariant to such adiabatic changes of the Hamiltonian parameters is the total entropy per particle of the quantum gas $S/(Nk_B)$. Whether or not a specific many-body phase can thus be reached via adiabatic change of system parameters is only a question of whether the initial entropy of the initial system is low enough. For example, experiments typically begin with a fermionic or bosonic quantum gas cooled via evaporative cooling to a certain temperature in the harmonic trapping potential of a magnetic or an optical dipole trap. This temperature determines the entropy of the quantum gas. Then optical lattices are turned on by increasing the intensity of the corresponding light fields. Under the assumption of adiabatic changes of the lattice potential, the entropy of the systems remains constant. Typically experiments are

carried out under this assumption of conserved entropy, however it is not always fulfilled, as timescales for reaching equilibrium in interacting many-body systems have been shown to increase with interaction strength [55–57].

4.1 Bose-Hubbard Model

The theory proposal [53, 58] and the subsequent realization of the Bose-Hubbard model with ultracold atoms [59] marks the starting point for strong correlation physics with ultracold quantum gases. Within this model, a gas of interacting bosons occupying the lowest Bloch band of a periodic potential forms a superfluid below a critical ratio of interaction to kinetic energy ($U/J < (U/J)_c$). For integer filling of the lattice and for $U/J > (U/J)_c$, the system turns into a strongly correlated Mott insulator. By increasing the optical lattice depth, the ratio of interaction to kinetic energy of the system U/J can be tuned to increasingly large values. Even without employing scattering resonances to tune U , it is thus possible to bring the bosonic quantum gas into a strongly correlated regime of a Mott insulator simply by quenching the kinetic energy of the system. The transition from a superfluid to a Mott insulator has by now been the focus of numerous theoretical and experimental investigations and it is beyond the scope of this article to give a complete survey of these. The interested reader may find more detailed reviews on the topic in Refs. [1–3].

In the following, we will instead try to highlight a few characteristic properties that exemplify the dramatic changes occurring when the quantum gas is converted from a superfluid into a Mott insulator. Among one of the most prominent features are the measurement on the change of coherence properties when the transition is crossed. For a superfluid state, the underlying condensate exhibits long-range phase coherence and thus shows sharp matter wave interference peaks when the quantum gas is released from the optical lattice. Deep in the Mott insulating phase $U/J \gg (U/J)_c$, the system is comprised of pure Fock states of integer on-site density and thus no interference pattern is observed [59]. For finite tunneling, particle-hole fluctuations induced by the kinetic energy of the quantum gas, can allow even a Mott insulator to exhibit finite coherence properties [33]. However, as the particle-hole pairs are created only on nearest neighbor lattice sites, this coherence is rather short ranged in nature and distinctly different from the long-range phase coherence of a BEC. As the transition point to the superfluid is approached, the particle-hole pairs begin to extend over larger and larger distances, eventually becoming deconfined and inducing the formation of a superfluid at the transition point [60]. It is thus natural to view the Mott insulator as a gas of bound particle-hole pairs, on top of a fixed density background.

The harmonic trapping potential that is typical in cold atom experiments and is present in addition to the periodic potential, plays a crucial role for the realization of strongly interacting quantum phases on a lattice. Whereas for a homogeneous system one would need to tune the filling to integer values to observe the transition to a Mott insulator, the density distribution in a trap can change and the formation

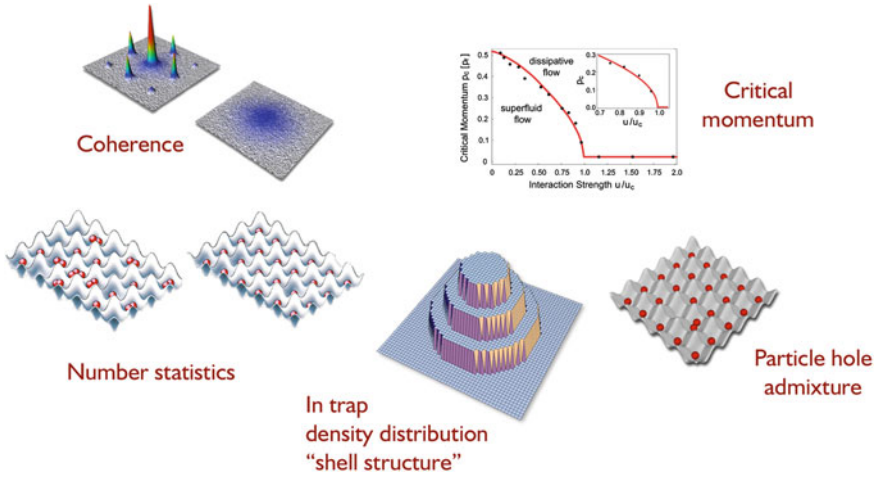


Fig. 6 Summary of phenomena that have been measured in the context of the Bose-Hubbard model. Several characteristic properties in the transition from a superfluid to a Mott insulator have been investigated experimentally. Among these are the different coherence properties, number statistics, density distributions and transport properties

of a Mott insulator can be induced even for an initially non-commensurate lattice density. In fact, as the lattice is raised, Mott insulating regions will automatically form in the trap for low enough temperatures. These Mott insulating regions become visible as constant integer density plateaus, with jumps in density at characteristic trap radii. The resulting density distribution of a Mott insulator therefore resembles a 'wedding cake' type structure in the trap (see Fig. 6). The regions of constant density are characteristic for the incompressible nature of the Mott state with vanishing compressibility $\kappa = dn/d\mu = 0$. The compressibility of the quantum gas can also be related to the density fluctuations, for which one finds [61]:

$$k_B T \frac{\partial n}{\partial \mu} = \int \langle \hat{n}(\mathbf{r}) \hat{n}(\mathbf{r}') \rangle - \langle \hat{n}(\mathbf{r}) \rangle \langle \hat{n}(\mathbf{r}') \rangle d^3 r'. \quad (16)$$

For a system with short ranged density fluctuations (such as a Mott insulator), the right hand side of the equation takes essentially only non-zero values for $\mathbf{r} = \mathbf{r}'$ and thus corresponds to the on-site density fluctuations. The on-site number fluctuations of the quantum gas thus closely track the compressibility of the many-body state and may be used as an alternative way to identify the incompressible regions of a Mott insulator. The wedding cake structure of the density distribution including Mott plateaus have been revealed in several experiments [62–65]. In the most recent measurements using single-atom and single-site resolved detection of atoms in optical lattice that are discussed in Sect. 6, the vanishing number fluctuations were also directly observed at the single-site level [64, 65].

4.2 Fermi-Hubbard Model

Restricting our discussion to the lowest energy band of a simple cubic 3D optical lattice, a fermionic quantum gas mixture can be modeled via the Hubbard-Hamiltonian [66] with an additional term describing the underlying harmonic potential:

$$\begin{aligned} \hat{H} = & -J \sum_{\langle \mathbf{R}, \mathbf{R}' \rangle, \sigma} \hat{a}_{\mathbf{R}, \sigma}^\dagger \hat{a}_{\mathbf{R}', \sigma} + U \sum_{\mathbf{R}} \hat{n}_{\mathbf{R}, \downarrow} \hat{n}_{\mathbf{R}, \uparrow} \\ & + V_t \sum_{\mathbf{R}, \sigma} \mathbf{R}^2 \hat{n}_{\mathbf{R}, \sigma}. \end{aligned} \quad (17)$$

The quantum phases of the fermionic Hubbard model with harmonic confinement are governed by the interplay between three energy scales: kinetic energy, whose scale is given by the lattice bandwidth $12J$, interaction energy U , and the strength of the harmonic confinement, which can conveniently be expressed by the characteristic trap energy $E_t = V_t(N_\sigma/(4\pi/3))^{2/3}$, denoting the Fermi-energy of a non-interacting cloud in the zero-tunneling limit, with N_σ being the number of atoms per spin state ($N_\downarrow = N_\uparrow$). The characteristic trap energy depends both on atom number and trap frequency via $E_t \propto \omega_\perp^2 N_\sigma^{2/3}$ and describes the effective compression of the quantum gas, controlled by the trapping potential in the experiment.

Depending on which term in the Hamiltonian dominates, different kinds of many-body ground states can occur in the trap center. For weak interactions in a shallow trap $U \ll E_t \ll 12J$ the Fermi energy is smaller than the lattice bandwidth ($E_F < 12J$) and the atoms are delocalized in order to minimize their kinetic energy. This leads to compressible metallic states with central filling $n_{0, \sigma} < 1$, where the local filling factor $n_{\mathbf{R}, \sigma} = \langle \hat{n}_{\mathbf{R}, \sigma} \rangle$ denotes the average occupation per spin state of a given lattice site. A dominating repulsive interaction $U \gg 12J$ and $U \gg E_t$ suppresses the double occupation of lattice sites and can lead to Fermi-liquid ($n_{0, \sigma} < 1/2$) or Mott-insulating ($n_{0, \sigma} = 1/2$) states at the trap center, depending on the ratio of kinetic to characteristic trap energy. Stronger compressions lead to higher filling factors, ultimately ($E_t \gg 12J, E_t \gg U$) resulting in an incompressible band insulator with unity central filling at $T = 0$.

Finite temperature reduces all filling factors and enlarges the cloud size, as the system needs to accommodate the corresponding entropy. Furthermore, in the trap the filling always varies smoothly from a maximum at the center to zero at the edges of the cloud. For a dominating trap and strong repulsive interaction at low temperature ($E_t > U > 12J$), the interplay between the different terms in the Hamiltonian gives rise to a wedding-cake like structure consisting of a band-insulating core ($n_{0, \sigma} \approx 1$) surrounded by a metallic shell ($1/2 < n_{\mathbf{R}, \sigma} < 1$), a Mott-insulating shell ($n_{\mathbf{R}, \sigma} = 1/2$) and a further metallic shell ($n_{\mathbf{R}, \sigma} < 1/2$) [67]. The outermost shell remains always metallic, independent of interaction and confinement, only its thickness varies.

Recent experiments on ultracold fermionic spin mixtures of ^{40}K atoms have been able to reach a paramagnetic Mott insulating phase for increasing interactions in the

quantum gases in the range of $U/(12J) \simeq 1.5 - 4$ [68, 69]. In the experiments, the suppression of double occupancy (doublons) or the incompressible nature of an insulating phase have been used in order to identify the Mott insulating phase. For example for $k_B T < U$ and strong interactions, one expects doubly occupied sites $D = \langle \hat{n}_{\mathbf{R},\uparrow} \hat{n}_{\mathbf{R},\downarrow} \rangle / (\langle n_{\mathbf{R},\uparrow} \rangle + \langle n_{\mathbf{R},\downarrow} \rangle)$ to be strongly suppressed compared to the non-interacting case [70]. Furthermore when the system is in an insulating phase, the compressibility of the system will drop to a minimum. Both these quantities can be compared to ab-initio Dynamical Mean Field Theory (DMFT) calculations [69, 71]. As the lowest achieved temperatures of the quantum gases are still above the single particle hopping $k_B T \gtrsim J$, a high temperature series expansion of the partition function has also been shown to be useful for comparison with the experimental results [71, 72]. The detailed comparison with theory has allowed one extract the entropies per particle of current experiments being in the range of $S/N = (1 - 1.8) k_B$, for which Mott insulating behavior could be observed. Interestingly, for the upper limit values, these entropies are larger than the maximum entropy that can be stored in a homogeneous single band Hubbard model system of $S_{\max}/N = k_B 2 \log 2$. For a homogeneous system, one would thus not expect the system to show Mott insulating behavior, however, for the trapped quantum gas the entropy per particle is distributed inhomogeneously throughout the system, such that in the metallic wings the excess entropy above $S/N = k_B \log 2$ can be efficiently stored as configurational entropy of the particles. This inhomogeneous entropy distribution is in fact key to novel cooling (or better entropy reduction) methods that have been proposed for ultracold atoms in optical lattices [73, 74].

Simulating the repulsive model with a system of attractively interacting particles ($U < 0$) has recently been shown to exhibit advantages, especially when one wants to probe the effects of a controlled doping of e.g. an antiferromagnetic Mott insulator [75]. For fermions with attractive interactions a preformed paired phase has been detected [76], however, the generation of a superfluid state within the single band has not yet been achieved. The temperatures (and entropies) required to realize such a state are in fact comparable to the ones required for an antiferromagnet in the repulsive Hubbard model [77].

5 Quantum Magnetism with Ultracold Atoms in Optical Lattices

Magnetically ordered quantum phases play an important role in the low-temperature regime of the Hubbard model. The underlying spin-spin interactions responsible for the magnetically ordered phases arise due to superexchange mediated coupling of neighbouring spins and our primary goal will be to understand, how such superexchange couplings emerge in two-component quantum gases on a lattice in the regime of strong interactions. For this, it will be useful to first introduce a 'toy model' of two spins in a double well—a system that can be in effect realized in the lab using superlattice potentials and that plays an important role in the context of realizing solid state qubits in electronic double well quantum dots. Extensions of these results

to larger plaquette sized systems and the formation of resonating valence bond states will also be discussed.

5.1 Superexchange Spin Interactions

5.1.1 Superexchange Interactions in a Double Well

Spin-Spin interactions between neighbouring atoms are mediated via so called superexchange processes. They directly arise from within the Hubbard model in the regime of strong interactions, leading to an effective Hamiltonian that couples the spin of neighbouring atoms in a lattice. Let us first discuss how such superexchange interactions can be derived theoretically (see also [78]). As a starting point, we discuss the case of an atom with spin-up $|\uparrow\rangle$ and another atom with $|\downarrow\rangle$ loaded into a double well potential. In the regime of strong repulsive interactions $U \gg J$, doubly occupied sites are energetically suppressed and our system can be described by the following basis states of the left and right well $\mathcal{S} = \{|\downarrow, \uparrow\rangle, |\uparrow, \downarrow\rangle, |\uparrow, \uparrow\rangle, |\downarrow, \downarrow\rangle\}$.

The action of the tunneling operator of the Hubbard Hamiltonian can be evaluated in the strongly interacting regime via perturbation theory. First order tunneling processes lead out of the energetically allowed subspace and are therefore forbidden. However, second order tunneling processes that leave the system within \mathcal{S} lead to an effective coupling between the different spin states. We can describe such processes via an effective Hamiltonian of the system, whose matrix elements within \mathcal{S} can be evaluated via second order perturbation theory:

$$H_{a,b}^{\text{eff}} = -\langle a|\hat{H}_J \frac{1 - \hat{P}_{\mathcal{S}}}{U} \hat{H}_J|b\rangle = -\sum_{n \notin \mathcal{S}} \langle a|\hat{H}_J|n\rangle \frac{1}{\langle n|\hat{H}^{\text{int}}|n\rangle} \langle n|\hat{H}_J|b\rangle. \quad (18)$$

Here \hat{H}^J denotes the tunnelling and \hat{H}^{int} the interaction part of the Hubbard Hamiltonian and $\hat{P}_{\mathcal{S}}$ represents the projector into the subspace \mathcal{S} .

Let us consider for example the process that can lead to an exchange of two spins (see also Fig. 7):

$$\begin{aligned} |\downarrow, \uparrow\rangle &\xrightarrow{J} \overbrace{|\downarrow, \uparrow\rangle}^{-1/U} \xrightarrow{J} |\uparrow, \downarrow\rangle \\ \text{or } |\uparrow, \downarrow, 0\rangle &\xrightarrow[-1/U]{J} |\uparrow, \downarrow\rangle \end{aligned} \quad (19)$$

The two possible pathways thus sum up to an effective coupling strength $-J_{\text{ex}} = -2J^2/U$. Evaluating the other matrix elements in the same way, we obtain for the case of bosonic atoms the following matrix form of H^{eff} in the basis \mathcal{S} :

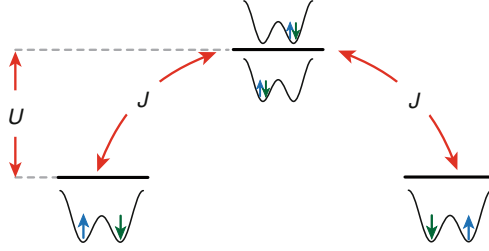


Fig. 7 Schematic of superexchange interactions in a double well. For the case of strong repulsive interactions between the particles, atoms can mediate interactions between neighbouring sites via second order tunneling processes, depicted in the image. The second order hopping of the particles via an intermediate state can lead to an exchange of the spins in the system

$$H_{\text{bosons}}^{\text{eff}} = J_{\text{ex}} \begin{pmatrix} -1 & -1 & 0 & 0 \\ -1 & -1 & 0 & 0 \\ 0 & 0 & -1 & 0 \\ 0 & 0 & 0 & -1 \end{pmatrix} \quad (20)$$

Diagonalizing the effective Hamiltonian yields the new eigenstates and eigenenergies:

$$\{|t_+\rangle, |t_0\rangle, |t_-\rangle\} \quad \text{with} \quad E = -2J_{\text{ex}} \quad (21)$$

$$|s_0\rangle \quad \text{with} \quad E = 0. \quad (22)$$

Here $|t_+\rangle = |\uparrow, \uparrow\rangle$, $|t_-\rangle = |\downarrow, \downarrow\rangle$, and $|t_0\rangle = 1/\sqrt{2}(|\downarrow, \uparrow\rangle + |\uparrow, \downarrow\rangle)$ are the spin-triplet eigenstates, whereas $|s_0\rangle = 1/\sqrt{2}(|\downarrow, \uparrow\rangle - |\uparrow, \downarrow\rangle)$ denotes the spin-singlet eigenstate of the two atoms. We may thus write \hat{H}^{eff} via a projector into the spin-triplet subspace \hat{P}_T , as:

$$\hat{H}^{\text{eff}} = -2J_{\text{ex}}\hat{P}_T = -J_{\text{ex}}\left(\hat{1} + \hat{X}_{LR}\right), \quad (23)$$

where \hat{X}_{LR} denotes the exchange operator between the left and right well. The projection operator into the singlet and triplet subspace can be expressed via Dirac notation as:

$$P_T = \frac{3}{4} + \hat{S}_L \cdot \hat{S}_R. \quad (24)$$

We can thus write the effective Hamiltonian as an interaction term between spins on the neighbouring wells:

$$H^{\text{eff}} = -2J_{\text{ex}}\hat{S}_L \cdot \hat{S}_R. \quad (25)$$

The minus sign for the case of bosons indicates ferromagnetic interactions, as the energy of the two spins is lowered if they align along the same direction.

For the case of fermionic spin mixtures, we can essentially follow the same derivation, however for equal spin on neighbouring sites, second order hopping processes are forbidden, due to Pauli blocking in the intermediate state, where both particles with identical spin would occupy the same spin state. Also, when two particles are exchanged, we obtain an additional minus sign in the coupling owing to the odd exchange symmetry of fermionic particles. The effective Hamiltonian for fermions thus reads:

$$H_{\text{fermions}}^{\text{eff}} = J_{\text{ex}} \begin{pmatrix} -1 & 1 & 0 & 0 \\ 1 & -1 & 0 & 0 \\ 0 & 0 & 0 & 0 \\ 0 & 0 & 0 & 0 \end{pmatrix} \quad (26)$$

Diagonalizing the effective Hamiltonian in the fermionic case yields the eigenstates and eigenenergies:

$$\{|t_+\rangle, |t_0\rangle, |t_-\rangle\} \quad \text{with} \quad E = 0 \quad (27)$$

$$|s_0\rangle \quad \text{with} \quad E = -2J_{\text{ex}}. \quad (28)$$

For fermions the spin-singlet state $|s_0\rangle$ is thus lower in energy and antiparallel orientation of the spins is thus favored. For the effective Hamiltonian we therefore obtain

$$\hat{H}^{\text{eff}} = -2J_{\text{ex}}\hat{P}_S = -J_{\text{ex}}(\hat{1} - \hat{X}_{LR}). \quad (29)$$

Making use of

$$P_S = \frac{1}{4} - \hat{S}_L \cdot \hat{S}_R. \quad (30)$$

we obtain for the fermionic spin Hamiltonian in the case of a double (up to a constant)

$$H^{\text{eff}} = +2J_{\text{ex}}\hat{S}_L \cdot \hat{S}_R, \quad (31)$$

favouring antiferromagnetic ordering between the particles. It is interesting to remind ourselves that the interactions between particles on neighbouring sites purely arise due to the strong repulsive contact interaction between the particles, virtual hopping of the spins and the exchange symmetry of the resulting quantum states. No long ranged interactions are required to yield these interactions on neighbouring lattice sites.

5.1.2 Superexchange Interactions on a Lattice

Our above derivation can be extended to the case of a lattice system in a straightforward manner. For a bosonic or fermionic quantum system consisting of an equal mixture of two spin components in a Mott insulating regime with $\langle \hat{n}_{i,\uparrow} \rangle + \langle \hat{n}_{i,\downarrow} \rangle = 1$ and low enough temperatures, one expects magnetically ordered quantum phases

due to such superexchange spin-spin interactions. In the simplest case, such spin interactions take the form of an isotropic Heisenberg model:

$$H = \pm J_{ex} \sum_{\langle \mathbf{R}, \mathbf{R}' \rangle} \hat{\mathbf{S}}_{\mathbf{R}} \cdot \hat{\mathbf{S}}_{\mathbf{R}'}, \quad (32)$$

with effective spin-1/2 operators $\hat{S}_{\mathbf{R}}^x = (\hat{a}_{\mathbf{R},\uparrow}^\dagger \hat{a}_{\mathbf{R},\downarrow} + \hat{a}_{\mathbf{R},\downarrow}^\dagger \hat{a}_{\mathbf{R},\uparrow})/2$, $\hat{S}_{\mathbf{R}}^y = (\hat{a}_{\mathbf{R},\uparrow}^\dagger \hat{a}_{\mathbf{R},\downarrow} - \hat{a}_{\mathbf{R},\downarrow}^\dagger \hat{a}_{\mathbf{R},\uparrow})/2i$ and $\hat{S}_{\mathbf{R}}^z = (\hat{n}_{\mathbf{R},\uparrow} - \hat{n}_{\mathbf{R},\downarrow})/2$ and exchange coupling constant $J_{ex} = 2J^2/U$.

It is instructive to re-write the Heisenberg Hamiltonian using the spin raising and lowering operators $\hat{S}_{\mathbf{R}}^+ = (\hat{S}_{\mathbf{R}}^x + i\hat{S}_{\mathbf{R}}^y) = \hat{a}_{\mathbf{R},\uparrow}^\dagger \hat{a}_{\mathbf{R},\downarrow}$ and $\hat{S}_{\mathbf{R}}^- = (\hat{S}_{\mathbf{R}}^x - i\hat{S}_{\mathbf{R}}^y) = \hat{a}_{\mathbf{R},\downarrow}^\dagger \hat{a}_{\mathbf{R},\uparrow}$. We find:

$$H = \pm \frac{J_{ex}}{2} \sum_{\langle \mathbf{R}, \mathbf{R}' \rangle} \left(\hat{S}_{\mathbf{R}}^+ \hat{S}_{\mathbf{R}'}^- + \hat{S}_{\mathbf{R}}^- \hat{S}_{\mathbf{R}'}^+ \right) \pm \frac{J_{ex}}{2} \sum_{\langle \mathbf{R}, \mathbf{R}' \rangle} \hat{S}_{\mathbf{R}}^z \hat{S}_{\mathbf{R}'}^z \quad (33)$$

Note that in this form it becomes especially apparent that the first part of the spin Hamiltonian has exactly the same structure as the tunneling operator in the Hubbard Hamiltonian, while the second term acts like nearest neighbour interaction term.

5.2 Tunable Superexchange Interactions

Let us turn to the more general case of spin-spin interactions in two-component Bose-Bose or Fermi-Fermi mixtures in the strong coupling regime and half filling, but in general unequal hopping matrix elements $J_\sigma \neq J_{\sigma'}$ and tunable interspecies and intraspecies interactions $U_{\uparrow\downarrow}$ and $U_{\sigma\sigma}$ (for fermions in a single-band model $U_{\sigma\sigma} = 0$). In this case one finds an XXZ-type spin Hamiltonian of the form [79, 80]:

$$H = \sum_{\langle \mathbf{R}, \mathbf{R}' \rangle} \left[J_{ex}^z \hat{S}_{\mathbf{R}}^z \hat{S}_{\mathbf{R}'}^z \pm J_{ex}^\perp \left(\hat{S}_{\mathbf{R}}^x \hat{S}_{\mathbf{R}'}^x + \hat{S}_{\mathbf{R}}^y \hat{S}_{\mathbf{R}'}^y \right) \right], \quad (34)$$

with tunable exchange coefficients for bosonic particles:

$$J_{ex}^z = \frac{J_\uparrow^2 + J_\downarrow^2}{U_{\uparrow\downarrow}} - \frac{2J_\uparrow^2}{U_{\uparrow\uparrow}} - \frac{2J_\downarrow^2}{U_{\downarrow\downarrow}} \quad \text{and} \quad J_{ex}^\perp = \frac{2J_\uparrow J_\downarrow}{U_{\uparrow\downarrow}}. \quad (35)$$

For fermionic atoms, the expression for J_{ex}^\perp is identical, however in the expression for J_{ex}^z the last two terms vanish. By tuning the different interaction matrix elements,

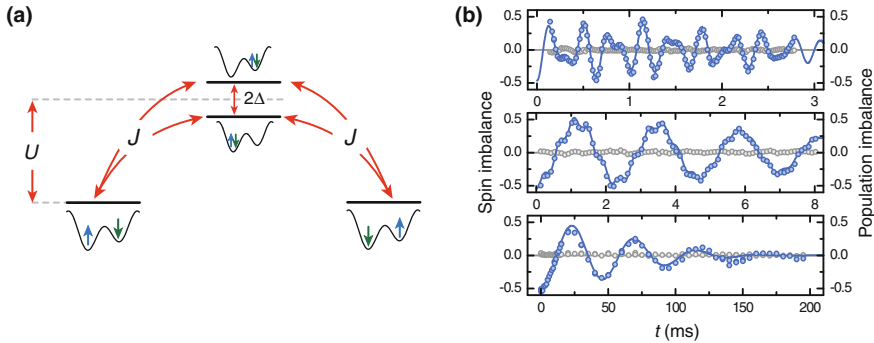


Fig. 8 Detecting and Controlling Superexchange Interactions **(a)** Superexchange interactions are mediated via second order hopping processes. By introducing an energy offset Δ between neighboring lattice sites, one may tune the exchange coupling J_{ex} . **(b)** Dynamical observation of superexchange interaction in double wells, initially prepared in a z -Néel order (see **a**). For increasing interactions (*top row to bottom row*) one observes how Heisenberg type superexchange spin-spin interactions emerge and single particle hopping becomes increasingly suppressed due to the increased repulsive interactions between the particles. Adapted from Trotzky et al. [28]

e.g. via Feshbach resonances, or by tuning the different hopping matrix element, one may thus easily tune the system from an Ising type interacting over a isotropic Heisenberg interaction to a dominating transverse spin-spin interaction.

Time resolved superexchange interactions between ultracold atoms have been observed with ultracold bosons in optical double well setups using optical superlattices (see Fig. 8). By introducing an energy offset Δ between neighboring lattice sites, Trotzky et al. [28] showed that the superexchange coupling can be tuned via $J_{ex} = J^2/(U + \Delta) + J^2/(U - \Delta)$. When $\Delta > U$ the sign of the superexchange coupling is thus reversed, allowing one to tune between ferromagnetic and antiferromagnetic spin interactions of the particles. It is thus also conceivable to generate quantum systems, for which ferromagnetic and antiferromagnetic spin interactions are simultaneously present along different lattice axes.

5.3 Resonating Valence Bond States in a Plaquette

The concept of valence bond resonance plays a fundamental role in the theory of the chemical bond [81, 82] and is believed to lie at the heart of many-body quantum physical phenomena [83, 84]. By making use of optical superlattices in two orthogonal directions, it has recently become possible to create such resonating valence bond (RVB) states of different symmetry types in arrays of plaquettes (see Fig. 9) [29, 30]. In the experiment, one could for example begin with spin singlets along the vertical direction (A-D and B-C in Fig. 9a) with suppressed exchange coupling

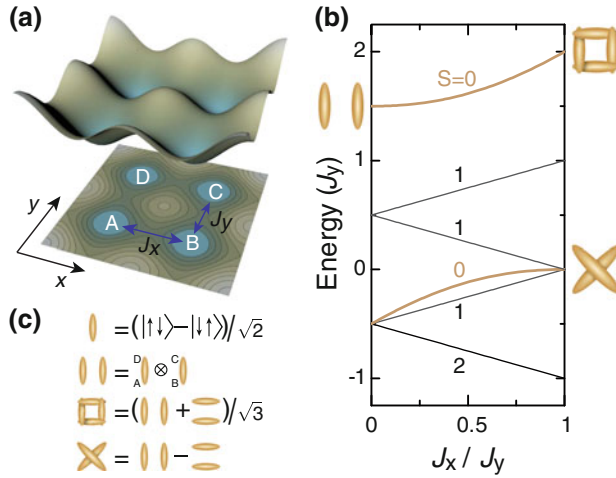


Fig. 9 Schematics of a single plaquette and energy levels at half filling. **a** Scheme of the lattice potential in the x, y plane, created by a pair of bichromatic optical lattices. The elementary cell is made of four wells arranged in a *square* configuration. **b** Energy levels of four atoms on a plaquette in a Mott insulating state at half filling, with superexchange spin couplings along x (y) denoted by J_x (J_y). For any ratio J_x/J_y , the highest energy state is a total spin- $\frac{1}{2}$ singlet. In the case of $J_x/J_y = 0$, it corresponds to the valence bond state with singlets aligned along the vertical direction, whereas for $J_x/J_y = 1$ it is the s -wave RVB state. The other total singlet for $J_x = J_y$, lower in energy, is the d -wave RVB state, with singlets along the diagonals. **(c)** Symbols used for a singlet bond and for the s -wave and d -wave plaquette RVB states. From Nascimbene et al. [30]

in the horizontal direction, i.e. $J_x = 0$. By adiabatically turning on the exchange coupling in the horizontal direction to a point where $J_x = J_y$, the state could be transformed into a RVB state with s -wave symmetry. Such a state can be viewed as a coherent superposition of spin singlets in the horizontal and vertical direction, very much in analogy to the electronic binding configuration in a benzene molecule. If the exchange coupling along the horizontal direction was turned on abruptly to $J_x = J_y$, however, the systems started to exhibit valence bond oscillations between the two configurations where the singlets are oriented along the vertical and horizontal direction. Using more elaborate preparation techniques it has also been possible to realize RVB states with d -wave symmetry [29, 30].

Having such control possibilities at hand for the local creation of plaquette RVB state opens the path for coupling these plaquettes to larger system sizes and thereby extending the RVB state over a larger area of the two-dimensional spin system. Different protocols for achieving this have been discussed in the literature [31, 32].

6 Single-Site and Single-Atom Resolved Imaging and Addressing of Quantum Gases in Optical Lattices

Imaging single quantum particles has revolutionized the field of quantum optics. For several years, researchers have aspired to employ such single particle detection methods for the analysis of ultracold quantum gases. Only recently it has become possible to realize such imaging techniques, marking a milestone for the characterization and manipulation of ultracold quantum gases [64, 65, 85, 86]. In our discussion, we will focus on a novel detection employing high-resolution imaging of strongly interacting quantum gases. The imaging of a bosonic Mott insulator will serve as an example of the novel analyses possibilities available with this technique.

6.1 High Resolution and Single-Atom Sensitive Fluorescence Imaging

One of the standard imaging techniques in ultracold quantum gases—absorption imaging—cannot be easily extended to the regime of single atom sensitivity. This is mainly due to the limited absorption a laser beam experiences when interacting with a single atom. For typical experimental conditions, this absorption is smaller than the accompanying photon shot noise. While high resolution images of down to $1\mu\text{m}$ resolution have been successfully used to record *in-situ* absorption images of trapped quantum gases [63], they have not reached the single-atom sensitive detection regime. Fluorescence imaging can however overcome this limited signal-to-noise and therefore provides a viable route for combining high-resolution imaging with single-atom sensitivity. By using laser induced fluorescence and by trapping the atoms in a very deep potential, several hundred thousand photons can be scattered from a single atom, of which a few thousand are ultimately detected. An excellent signal-to-noise in the detection of a single atom can therefore be achieved.

This idea was first pioneered for the case of optical lattices by the group of D. Weiss [87], who loaded atoms from a magneto optical trap into a three-dimensional lattice with a lattice constant of $6\mu\text{m}$ [87]. However, for typical condensed matter oriented experiments, such large spaced lattice are of limited use, due to their almost vanishing tunnel coupling between neighbouring wells. Extending fluorescence imaging to a regime where the resolution can be comparable to typical lattice spacings of $d = 500\text{ nm}$, thus requires microscope objectives working in the regime of large numerical apertures (NA), as the smallest resolvable distances in classical optics are determined by $\sigma = \lambda/(2\text{NA})$.

In recent publications, Bakr et al. [64, 86] and Sherson et al. [65] have demonstrated such high-resolution imaging and applied it to image the transition of a superfluid to a Mott insulator in 2D. In the experiments, 2D Bose-Einstein condensates were first created in tightly confining potential planes. Subsequently, the depth of a two-dimensional simple-cubic type lattice was increased, leaving the system either

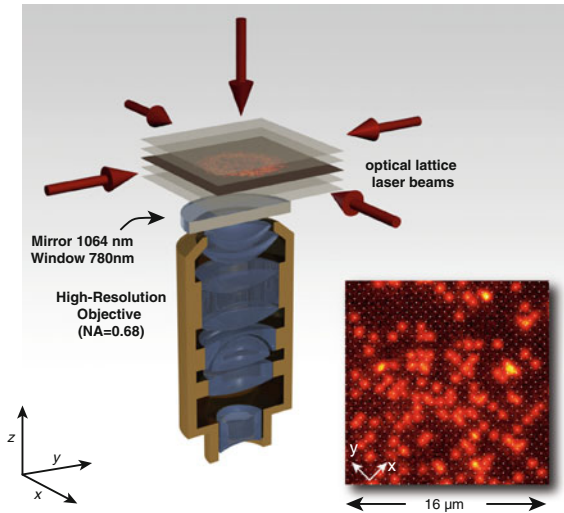


Fig. 10 Schematic setup for high resolution fluorescence imaging of a 2D quantum gas. Two-dimensional bosonic quantum gases are prepared in a single 2D plane of an optical standing wave along the z -direction, which is created by retro-reflecting a laser beam ($\lambda = 1064 \text{ nm}$) on the coated vacuum window. Additional lattice beams along the x - and y -directions are used to bring the system into the strongly correlated regime of a Mott insulator. The atoms are detected using fluorescence imaging via a high resolution microscope objective. Fluorescence of the atoms was induced by illuminating the quantum gas with an optical molasses that simultaneously laser cools the atoms. The *inset* shows a section from a fluorescence picture of a dilute thermal cloud (points mark the lattice sites). Adapted from Sherson et al. [65]

in a superfluid or Mott insulating regime. The lattice depths were then suddenly increasing to very deep values of $300 \mu\text{K}$, essentially freezing out the density distribution of the atoms in the lattice. A near-resonant optical molasses was then used to induce fluorescence of the atoms in the deep lattice. The molasses also provided laser cooling, such that atoms remained on lattice sites while fluorescing. High resolution microscope objectives with numerical apertures of $\text{NA} \approx 0.7 - 0.8$ were used to record the fluorescence and image the atomic density distribution on CCD cameras (see Fig. 10). A limitation of the detection method is that so called inelastic light-induced collision occurring during the illumination period only allow one to record the parity of the on-site atom number. Whenever pairs of atoms are present on a single lattice site, both atoms of the pair are rapidly lost within the first millisecond of illumination, due to a large energy release caused by radiative escape and fine-structure changing collisions [88].

In both experiments, high resolution imaging has allowed one to reconstruct the atom distribution (modulo 2) on the lattice down to a single-site level. Results for the case of a Bose-Einstein condensate and Mott insulators of such a digital particle number reconstruction are displayed in Fig. 11. The digitally reconstructed images have the significant advantage of essentially exhibiting an infinite signal-to-noise

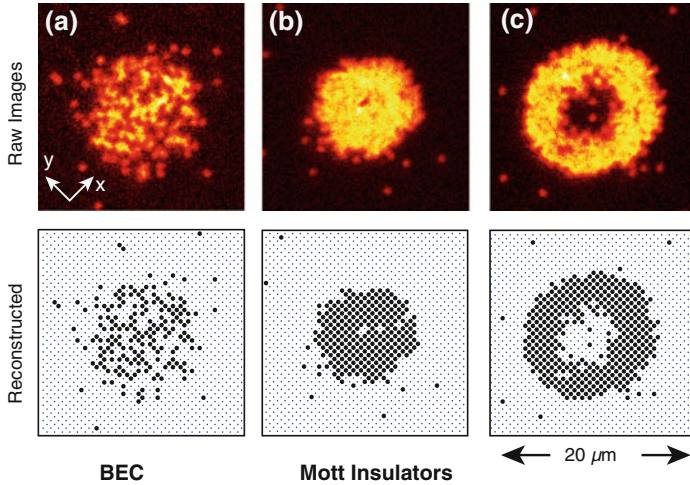


Fig. 11 High resolution fluorescence images of a weakly interacting Bose-Einstein condensate and Mott insulators. **a** Bose-Einstein condensate exhibiting large particle number fluctuations and **b**, **c** wedding cake structure of $n = 1$ and $n = 2$ Mott insulators. Using a numerical algorithm, the corresponding atom distribution on a lattice can be reconstructed. The reconstructed images can be seen in the row below (small points mark lattice sites, large points mark position of a single atom). Figure adapted from Sherson et al. [65]

ratio that is of great advantage in further correlation analyses. Non-local order parameters that are characteristic for topologically ordered quantum phases [89] can also be easily revealed with the detection method [60].

6.2 Thermodynamics of the Bose-Hubbard Model in the Atomic Limit

Modeling the density distribution and the fluctuations of the strongly interacting bosonic quantum gas becomes especially simple in the so called atomic limit of the Bose-Hubbard model, for which $J = 0$ or $U/J \rightarrow \infty$. In this limit the grand canonical partition function of the trapped quantum gas $Z^{(0)}$ can be written as a product of on-site partition functions:

$$Z^{(0)} = \prod_{\mathbf{R}} Z_{\mathbf{R}}^{(0)}, \quad (36)$$

where the on-site partition function is given by

$$Z^{(0)} = \sum_n e^{-\beta(E_n - \mu(\mathbf{R})n)}. \quad (37)$$

The local chemical potential at lattice site \mathbf{R} is denoted by $\mu(\mathbf{R})$ and the eigenenergy of n atoms on this lattice site is given by the standard single-band Bose-Hubbard interaction term $E_n = 1/2Un(n-1)$. In particular we can use the above to calculate the on-site probability of finding n atoms per lattice site as

$$P_{\mathbf{R}}(n) = \frac{e^{-\beta(E_n - \mu(\mathbf{R})n)}}{Z^{(0)}}. \quad (38)$$

We can thus think of our system as consisting of disconnected sites, whose thermodynamics is determined only by the ratio of $U/(k_B T)$ and the local chemical potential. In this limit the problem becomes analytically tractable and simple to analyze.

6.2.1 Radial Density and Fluctuation Profiles

As a simple application of our result, let us calculate the density profile and its fluctuations for a two-dimensional radially symmetric trapping potential. All sites with the same distance r from the trapping centre exhibit the same chemical potential $\mu(r)$. The average density at this radial distance is thus given by:

$$\bar{n} = \frac{1}{Z(r)} \sum_n n e^{-\beta(E_n - \mu(r)n)}. \quad (39)$$

In order to evaluate this, we would need to sum over all possible occupation states in our on-site partition function. In practice, we may truncate our sum around values of $\text{int}[\mu/U] \pm 1$ for temperatures $k_B T \ll U$, as thermal fluctuations become exponentially suppressed in this regime. This is the so called *particle-hole* approximation.

In the case of fluorescence imaging, light assisted collisions allow us to only detect the parity of the on-site atom number, i.e. the on-site particle number modulo 2. We thus find for the detected average density:

$$\bar{n}_{det} = \frac{1}{Z(r)} \sum_n \text{mod}_2(n) e^{-\beta(E_n - \mu(r)n)}. \quad (40)$$

For the fluctuations of the quantum gas, we find that due to the parity projection in the detection process $\overline{n^2(r)} = \bar{n}_{det}$, resulting in

$$\sigma_{det}^2(r) = \bar{n}_{det}(r) - \bar{n}_{det}^2(r). \quad (41)$$

for the detected fluctuations. Both the detected fluctuations and the average density profile are functions of three parameters μ/U , $k_B T/U$ and the trapping frequency ω^2 of the overall harmonic confinement. While the trap frequency can be independently measured, the chemical potential and temperature of the quantum gas can be

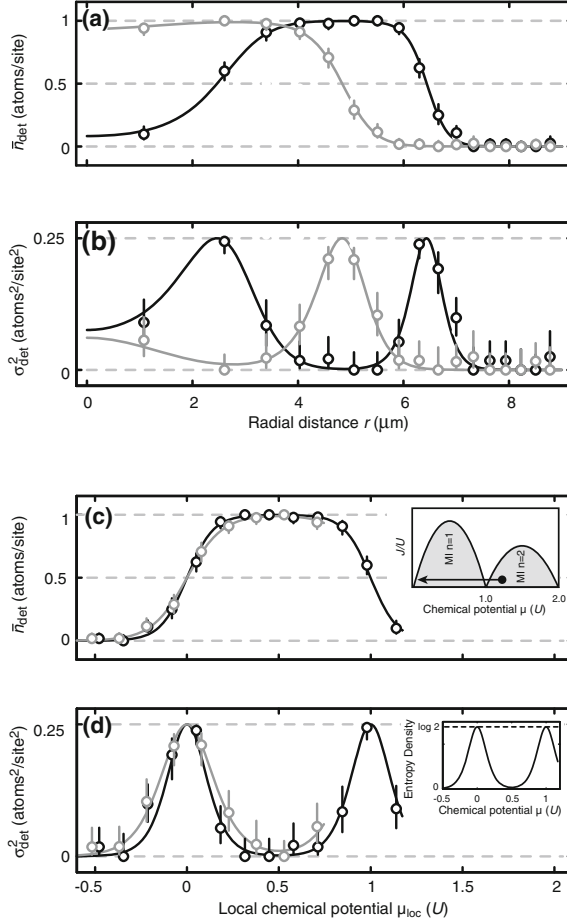


Fig. 12 Radial atom density and variance profiles. Radial profiles were obtained from the digitized reconstructed images by azimuthal averaging. **a, b**, grey and black points correspond to the $n = 1$ and $n = 2$ MI images of Fig. 11 d, e. For the two curves, the fits yielded temperatures $T = 0.090(5)U/k_B$ and $T = 0.074(5)U/k_B$, chemical potentials $\mu = 0.73(3)U$ and $\mu = 1.17(1)U$, and radii $r_0 = 5.7(1)\mu\text{m}$ and $r_0 = 5.95(4)\mu\text{m}$ respectively. From the fitted values of T , μ and r_0 , we determined the atom numbers of the system to $N = 300(20)$ and $N = 610(20)$. **c, d**, The same data plotted versus the local chemical potential using local-density approximation. The inset of **c** is a Bose-Hubbard phase diagram ($T = 0$) showing the transition between the characteristic MI lobes and the superfluid region. The line starting at the maximum chemical potential μ shows the part of the phase diagram existing simultaneously at different radii in the trap due to the external harmonic confinement. The inset of **d** is the entropy density calculated for the displayed $n = 2$ MI. From Sherson et al. [65]

extracted via a fit to azimuthally averaged radial density profiles of single images of the quantum gas. This is shown in Fig. 12 for the two images of an $n = 1$ and $n = 2$ Mott insulator in the core of the gas.

In the atomic limit, these fit-functions thus allow an efficient determination of temperature and chemical potential of the quantum gas. Note that apart from the particle-hole and local density approximation (LDA), no further approximations have to be made in this case, giving exact numerical model functions for the trapped Bose gas. The radial density and fluctuation profiles can be converted to density and fluctuation profiles versus chemical potential by using again LDA $\mu_{loc}(r) = \mu - 1/2 m\omega^2 r^2$. We see that both data for the two distinct data sets of the $n = 1$ and $n = 2$ Mott insulators fall on top of each other when plotting in this way, underlining the fact that radial profiles correspond to cuts through the phase diagram (see inset in Fig. 12c) of the Bose-Hubbard model. Residual small differences between the two curves can be attributed to the slightly different temperatures of the atom clouds. Interestingly, as in the case of fermionic atoms, one notes that fluctuations are concentrated to the border of the Mott insulating regions, where the system is superfluid for $T = 0$ and it becomes thermodynamically easiest to introduce fluctuations in this spatial region, where the energy to create an excitation is lowest.

6.3 Single-Site Resolved Addressing of Individual Atoms

Being able to spatially resolve single lattice sites in addition allows to manipulate atoms with single-site resolution. A laser beam can simply be sent through the high-resolution objective in reverse direction and focused onto the atoms, thereby making use of the high-resolution objective twice—for imaging and for addressing. The resulting spot size of the laser beam will then, however, still be on the order of a lattice spacing and for most applications too large in order to reliably address atoms on single lattice sites. One possibility to increase the spatial resolution is to make use of a resonance imaging technique: the focused laser is tuned to such a wavelength that it creates a differential energy shift between two internal hyperfine ground states of an atom. Global microwave radiation, resonant between these two states only at a certain spatial position in the focused beam, can then be used to control the spin state of the atom [90, 91]. The spatial resolution for the addressing of single atoms can thereby be increased by almost an order of magnitude down to approx. 50 nm, well below the diffraction limit.

In the experiment, such addressing was demonstrated in a 2D Mott insulator with unity occupation per lattice site [91]. In order to prepare an arbitrary pattern of spins in the array, the laser beam was moved to a specific site and a Landau-Zener microwave sweep applied in order to flip the spin of the atom located at the lattice site. The laser beam was then moved to the next lattice site and the procedure was repeated. In order to detect the resulting spin pattern, unflipped atoms were removed by applying a resonant laser beam that rapidly expelled these atoms from the trap [91]. The remaining spin-flipped atoms were then detected using standard high-resolution fluorescence imaging, as described above. The resulting spin patterns can be seen in Fig. 13, showing that almost arbitrary spin orderings can be produced in this way.

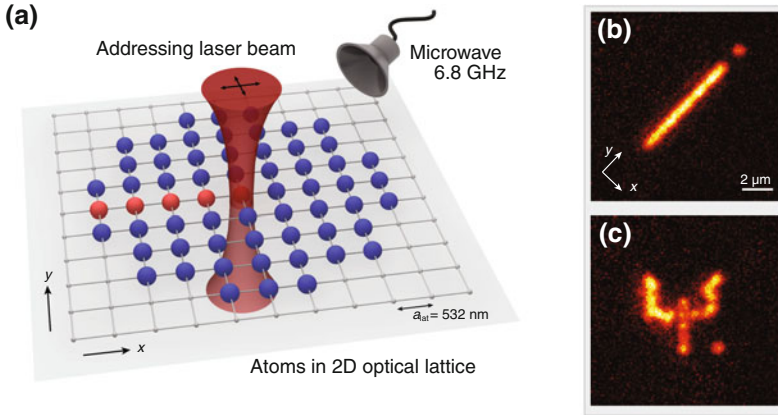


Fig. 13 High-resolution addressing of single atoms. **a** Atoms in a Mott insulator with unity filling arranged on a square lattice with period $a_{\text{lat}} = 532 \text{ nm}$ were addressed using an off-resonant laser beam. The beam was focussed onto individual lattice sites by a high-aperture microscope objective (not shown) and could be moved in the xy plane with an accuracy of better than $0.1 a_{\text{lat}}$. **b**, **c** Fluorescence images of spin-flipped atoms following the addressing procedure. From Weitenberg et al. [91]

In order to demonstrate that the addressing does not affect the motional state of the atoms on a lattice site, the tunneling of particles was investigated after an addressing sequence. First, a line of atoms in spin state $|\uparrow\rangle$ embedded in a bath of atoms in state $|\downarrow\rangle$ was prepared using a Mott insulator in a deep lattice, where tunneling is suppressed. Thereafter, the $|\downarrow\rangle$ atoms were removed through a resonant light pulse and the lattice depth along the x -direction was lowered in order to initiate tunneling of the particles asslong this direction. After a variable evolution time, the position of the atoms was measured (see Fig. 14a, b, c, d). By repeating the experiment several times, the probability of finding the atoms at a certain lattice site for a specific evolution time could be determined and compared to the probability distribution predicted by the Schrödinger equation for the quantum evolution of a single particle tunneling on a lattice. Excellent agreement was found between the experimental data and the theoretical prediction, indicating that most atoms indeed were still in the lower energy band of the lattice following the addressing. Atoms in higher energy bands typically exhibit an order of magnitude larger tunnel coupling, allowing them to travel much further given the same evolution time. However, in the experiment a negligible fraction of atoms was detected at such positions in the experiment.

High resolution imaging and addressing can be very useful for preparing almost arbitrary initial configurations of the many-body system that can e.g. be used to investigate a specific non-equilibrium evolution. It can also be highly beneficial

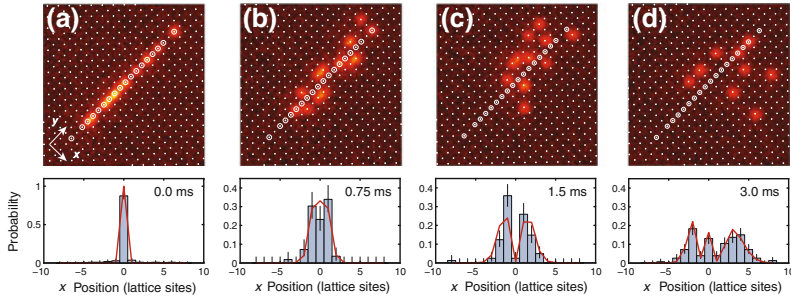


Fig. 14 Tunneling of single particles on a lattice. **a** Atoms were prepared in a single line along the y direction before the lattice along the x axis was lowered, allowing the atoms to tunnel in this direction (**b-d**). The *top row* shows snapshots of the atomic distribution after different hold times. *White circles* indicate the lattice sites at which the atoms were prepared (not all sites initially contained an atom). The *bottom row* shows the respective position distribution obtained from an average over 10–20 of such pictures, the error bars give the 1σ statistical uncertainty. The *red curve* corresponds to the prediction by theory. From Weitenberg et al. [91]

for quantum information applications, where e.g. in the case of a one-way quantum computer [92], it is essential to measure the spin state of an atom at a specified lattice site.

References

1. Jaksch, D., Zoller, P.: *Ann. Phys.* **315**, 52 (2005)
2. Lewenstein, M., Sanpera, A., Ahufinger, V., Damski, B., De, A.S., Sen, U.: *Adv. Phys.* **56**, 243 (2007)
3. Bloch, I., Dalibard, J., Zwerger, W.: *Rev. Mod. Phys.* **80**, 885 (2008)
4. Bloch, I., Dalibard, J., Nascimbène, S.: *Nat. Phys.* **8**, 267 (2012)
5. Chin, C., Grimm, R., Julienne, P., Tiesinga, E.: *Rev. Mod. Phys.* **82**, 1225 (2010)
6. Polkovnikov, A., Sengupta, K., Silva, A., Vengalattore, M.: *Rev. Mod. Phys.* **83**, 863 (2011)
7. Grimm, R., Weidemüller, M., Ovchinnikov, Y.: *Adv. At. Mol. Opt. Phys.* **42**, 95 (2000)
8. Peil, S., Porto, J., Laburthe-Tolra, B., Obrecht, J.M., King, B., Subbotin, M., Rolston, S., Phillips, W.: *Phys. Rev. A* **67**, 51603 (2003)
9. Hadzibabic, Z., Stock, S., Battelier, B., Bretin, V., Dalibard, J.: *Phys. Rev. Lett.* **93**, 180403 (2004)
10. Greiner, M., Bloch, I., Mandel, M.O., Hänsch, T.W., Esslinger, T.: *Phys. Rev. Lett.* **87**, 160405 (2001)
11. Moritz, H., Stöferle, T., Köhl, M., Esslinger, T.: *Phys. Rev. Lett.* **91**, 250402 (2003)
12. Tolra, B., O'Hara, K., Huckans, J., Phillips, W., Rolston, S., Porto, J.: *Phys. Rev. Lett.* **92**, 190401 (2004)
13. Paredes, B., Widera, A., Murg, V., Mandel, O., Fölling, S., Cirac, J.I., Shlyapnikov, G.V., Hänsch, T.W., Bloch, I.: *Nature* **429**, 277 (2004)
14. Kinoshita, T., Wenger, T., Weiss, D.: *Science* **305**, 1125 (2004)
15. Eckardt, A., Weiss, C., Holthaus, M.: *Phys. Rev. Lett.* **95**, 260404 (2005)
16. Lignier, H., Sias, C., Ciampini, D., Singh, Y., Zenesini, A., Morsch, O., Arimondo, E.: *Phys. Rev. Lett.* **99**, 220403 (2007)

17. Carr, L.D., DeMille, D., Krems, R.V., Ye, J.: New J. Phys. **11**, 055049 (2009)
18. Pupillo, G., Micheli, A., Boninsegni, M., Lesanovsky, I., Zoller, P.: Phys. Rev. Lett. **104**, 223002 (2010)
19. Honer, J., Weimer, H., Pfau, T., Büchler, H.-P.: Phys. Rev. Lett. **105**, 160404 (2010)
20. Henkel, N., Nath, R., Pohl, T.: Phys. Rev. Lett. **104**, 4 (2010)
21. Pollet, L., Prokofev, N., Svistunov, B.: Phys. Rev. Lett. **104**, 245705 (2010)
22. Becker, C., Soltan-Panahi, P., Kronjäger, J., Dörscher, S., Bongs, K., Sengstock, K.: New J. Phys. **12**, 065025 (2010)
23. Damski, B., Fehrmann, H., Everts, H.U., Baranov, M., Santos, L., Lewenstein, M.: Phys. Rev. A **72**, 053612 (2005)
24. Jaksch, D., Briegel, H.J., Cirac, J., Gardiner, C., Zoller, P.: Phys. Rev. Lett. **82**, 1975 (1999)
25. Mandel, O., Greiner, M., Widera, A., Rom, T., Hänsch, T.W., Bloch, I.: Phys. Rev. Lett. **91**, 10407 (2003)
26. Gadway, B., Pertot, D., Reimann, R., Schneble, D.: Phys. Rev. Lett. **105**, 045303 (2010)
27. Anderlini, M., Lee, P.J., Brown, B., Sebby-Strabley, J., Phillips, W., Porto, J.: Nature **448**, 452 (2007)
28. Trotzky, S., Cheinet, P., Fölling, S., Feld, M., Schnorrberger, U., Rey, A.M., Polkovnikov, A., Demler, E.a., Lukin, M.D., Bloch, I. Science **319**, 295 (2008)
29. Paredes, B., Bloch, I.: Phys. Rev. A **77**, 23603 (2008)
30. Nascimbène, S., Chen, Y.A., Atala, M., Aidelsburger, M., Trotzky, S., Paredes, B., Bloch, I.: Phys. Rev. Lett. **108**, 205301 (2012)
31. Trebst, S., Schollwöck, U., Troyer, M., Zoller, P.: Phys. Rev. Lett. **96**, 250402 (2006)
32. Rey, A.M., Sensarma, R., Fölling, S., Greiner, M., Demler, E., Lukin, M.D.: Europhys. Lett. **87**, 60001 (2009)
33. Gerbier, F., Widera, A., Fölling, S., Mandel, O., Gericke, T., Bloch, I.: Phys. Rev. Lett. **95**, 050404 (2005)
34. Gerbier, F., Trotzky, S., Fölling, S., Schnorrberger, U., Thompson, J., Widera, A., Bloch, I., Pollet, L., Troyer, M., Capogrosso-Sansone, B., Prokof'ev, N.V., Svistunov, B.V.: Phys. Rev. Lett. **101**, 155303 (2008)
35. Kastberg, A., Phillips, W., Rolston, S., Spreeuw, R., Jessen, P.: Phys. Rev. Lett. **74**, 1542 (1995)
36. Köhl, M., Moritz, H., Stöferle, T., Günter, K., Esslinger, T.: Phys. Rev. Lett. **94**, 80403 (2005)
37. Wirth, G., Ölschläger, M., Hemmerich, A.: Nat. Phys. **7**, 147 (2010)
38. Altman, E., Demler, E., Lukin, M.: Phys. Rev. A **70**, 13603 (2004)
39. Brown, Hanbury: R., Twiss, R. Nature **177**, 27 (1956).
40. Brown, Hanbury: R., Twiss, R. Nature **178**, 1447 (1956).
41. Baym, G.: Act. Phys. Pol. B **29**, 1839 (1998)
42. Henny, M., Oberholzer, S., Strunk, C., Heinzel, T., Ensslin, K., Holland, M., Schonenberger, C.: Science **284**, 296 (1999)
43. Oliver, W., Kim, J., Liu, R., Yamamoto, Y.: Science **284**, 299 (1999)
44. Kiesel, H., Renz, A., Hasselbach, F.: Nature **418**, 392 (2002)
45. Iannuzzi, M., Orecchini, A., Sacchetti, F., Facchi, P., Pascasio, S.: Phys. Rev. Lett. **96**, 80402 (2006)
46. Rom, T., Best, T., van Oosten, D., Schneider, U., Fölling, S., Paredes, B., Bloch, I.: Nature **444**, 733 (2006)
47. Jelte, T., McNamara, J., Hogervorst, W., Vassen, W., Krachmalnicoff, V., Schellekens, M., Perrin, A., Chang, H., Boiron, D., Aspect, A., Westbrook, C.: Nature **445**, 402 (2007)
48. Fölling, S., Gerbier, F., Widera, A., Mandel, O., Gericke, T., Bloch, I.: Nature **434**, 481 (2005)
49. Spielman, I., Phillips, W., Porto, J.: Phys. Rev. Lett. **98**, 080404 (2007)
50. Schellekens, M., Hoppeler, R., Perrin, A., Gomes, J., Boiron, D., Aspect, A., Westbrook, C.: Science **310**, 648 (2005)
51. Lee, P., Nagaosa, N., Wen, X.G.: Rev. Mod. Phys. **78**, 17 (2006)
52. Le Hur, K.: Maurice Rice. T. Ann. Phys. **324**, 1452 (2009)
53. Jaksch, D., Bruder, C., Cirac, J., Gardiner, C., Zoller, P.: Phys. Rev. Lett. **81**, 3108 (1998)
54. Hofstetter, W., Cirac, J., Zoller, P., Demler, E., Lukin, M.: Phys. Rev. Lett. **89**, 220407 (2002)

55. Strohmaier, N., Greif, D., Jördens, R., Tarruell, L., Moritz, H., Esslinger, T.: *Phys. Rev. Lett.* **104**, 080401 (2010)
56. Hung, C.L., Zhang, X., Gemelke, N., Chin, C.: *Phys. Rev. Lett.* **104**, 160403 (2010)
57. Schneider, U., Hackermüller, L., Ronzheimer, J., Will, S., Braun, S., Best, T., Bloch, I., Demler, E., Mandt, S., Rasch, D., Rosch, A.: *Nat. Phys.* **8**, 213–218 (2012)
58. Fisher, M.P.A., Weichman, P.B., Grinstein, G., Fisher, D.S.: *Phys. Rev. B* **40**, 546 (1989)
59. Greiner, M., Mandel, O., Esslinger, T., Hänsch, T.W., Bloch, I.: *Nature* **415**, 39 (2002)
60. Endres, M., Cheneau, M., Fukuhara, T., Weitenberg, C., Schauss, P., Gross, C., Mazza, L., Banuls, M.C., Pollet, L., Bloch, I., Kuhr, S.: *Science* **334**, 200 (2011)
61. Ho, T.L., Zhou, Q.: *Nat. Phys.* **6**, 131 (2009)
62. Fölling, S., Wiedera, A., Müller, T., Gerbier, F., Bloch, I.: *Phys. Rev. Lett.* **97**, 060403 (2006)
63. Gemelke, N., Zhang, X., Hung, C.L., Chin, C.: *Nature* **460**, 995 (2009)
64. Bakr, W.S., Peng, A., Tai, M., Ma, R., Simon, J., Gillen, J., Fölling, S., Pollet, L., Greiner, M.: *Science* **329**, 547 (2010)
65. Sherson, J.F., Weitenberg, C., Endres, M., Cheneau, M., Bloch, I., Kuhr, S.: *Nature* **467**, 68 (2010)
66. Hubbard, J.: *Proc. R. Soc. A* **276**, 238 (1963)
67. Helmes, R., Costi, T., Rosch, A.: *Phys. Rev. Lett.* **100**, 056403 (2008)
68. Jördens, R., Strohmaier, N., Günter, K., Moritz, H., Esslinger, T.: *Nature* **455**, 204 (2008)
69. Schneider, U., Hackermüller, L., Will, S., Bloch, I., Best, T., Costi, T., Helmes, R., Rasch, D., Rosch, A.: *Science* **322**, 1520 (2008)
70. DeLeo, L., Kollath, C., Georges, A., Ferrero, M., Parcollet, O.: *Phys. Rev. Lett.* **101**, 210403 (2008)
71. Jördens, R., Tarruell, L., Greif, D., Uehlinger, T., Strohmaier, N., Moritz, H., Esslinger, T., De Leo, L., Kollath, C., Georges, A., Scarola, V., Pollet, L., Burovski, E., Kozik, E., Troyer, M.: *Phys. Rev. Lett.* **104**, 180401 (2010)
72. Scarola, V.W., Pollet, L., Oitmaa, J., Troyer, M.: *Phys. Rev. Lett.* **102**, 135302 (2009)
73. Bernier, J.S., Kollath, C., Georges, A., De Leo, L., Gerbier, F., Salomon, C., Köhl, M.: *Phys. Rev. A* **79**, 061601(R) (2009)
74. Ho, T.L., Zhou, Q.: [arXiv:0911.5506](https://arxiv.org/abs/0911.5506) (2009).
75. Ho, A., Cazalilla, M., Giamarchi, T.: *Phys. Rev. A* **79**, 033620 (2009)
76. Hackermüller, L., Schneider, U., Moreno-Cardoner, M., Kitagawa, T., Best, T., Will, S., Demler, E., Altman, E., Bloch, I., Paredes, B.: *Science* **327**, 1621 (2010)
77. Paiva, T., Scalettar, R.T., Randeria, M., Trivedi, N.: *Phys. Rev. Lett.* **104**, 066406 (2010)
78. Auerbach, A.: *Interacting Electrons and Quantum Magnetism*. Springer, New York (1994)
79. Kuklov, A., Svistunov, B.: *Phys. Rev. Lett.* **90**, 100401 (2003)
80. Duan, L.M., Demler, E., Lukin, M.D.: *Phys. Rev. Lett.* **91**, 90402 (2003)
81. Pauling, L.: *J. Am. Chem. Soc.* **53**, 1367 (1931)
82. Hückel, E.: *Z. Phys. A* **70**, 204 (1931)
83. Anderson, P.: *Mat. Res. Bull.* **8**, 153 (1973)
84. Anderson, P.: *Science* **235**, 1196 (1987)
85. Gericke, T., Würtz, P., Reitz, D., Langen, T., Ott, H.: *Nat. Phys.* **4**, 949 (2008)
86. Bakr, W.S., Gillen, J.I., Peng, A., Fölling, S., Greiner, M.: *Nature* **462**, 74 (2009)
87. Nelson, K., Li, X., Weiss, D.: *Nat. Phys.* **3**, 556 (2007)
88. DePue, M.T.M., McCormick, C., Winoto, S.L., Oliver, S., Weiss, D.D.S.: *Phys. Rev. Lett.* **82**, 2262 (1999)
89. Wen, X.G.: *Quantum field theory of many-body systems*. In: *Oxford Graduate Texts*. Oxford University Press, Oxford (2004).
90. Weiss, D., Vala, J., Thapliyal, A., Myrgren, S., Vazirani, U., Whaley, K.: *Phys. Rev. A* **70**, 40302 (2004)
91. Weitenberg, C., Endres, M., Sherson, J.F., Cheneau, M., Schauß, P., Fukuhara, T., Bloch, I., Kuhr, S., Schauss, P.: *Nature* **471**, 319 (2011)
92. Raussendorf, R., Briegel, H.J.: *Phys. Rev. Lett.* **86**, 5188 (2001)

<http://www.springer.com/978-3-319-04062-2>

Quantum Information and Coherence

Andersson, E.; Öhberg, P. (Eds.)

2014, X, 285 p. 96 illus., 61 illus. in color., Hardcover

ISBN: 978-3-319-04062-2